Spin fluctuations after quantum quenches in the $S = 1$ Haldane chain: Numerical validation of the semi-semiclassical theory

Miklós Antal Werner,[1] Cătălin Paşcu Moca,[1,2] Örs Legeza,[3] Márton Kormos,[4] and Gergely Zaránd[1]

[1]*BME-MTA Exotic Quantum Phases Group, Institute of Physics, Budapest University of Technology and Economics,*
H-1111 Budapest, Hungary
[2]*Department of Physics, University of Oradea, 410087, Oradea, Romania*
[3]*Strongly Correlated Systems Lendület Research Group, Institute for Solid State Physics and Optics,*
MTA Wigner Research Centre for Physics, P.O. Box 49, H-1525 Budapest, Hungary
[4]*BME-MTA Statistical Field Theory Research Group, Institute of Physics,*
Budapest University of Technology and Economics, H-1111 Budapest, Hungary

We study quantum quenches in the $S = 1$ Heisenberg spin chain and show that the dynamics can be described by the recently developed semi-semiclassical method based on particles propagating along classical trajectories but scattering quantum mechanically. We analyze the nonequilibrium time evolution of the distribution of the total spin in half of the system and compare the predictions of the semi-semiclassical theory with those of a non-Abelian time-evolving block decimation (TEBD) algorithm which exploits the SU(2) symmetry. We show that while the standard semiclassical approach using the universal low-energy scattering matrix cannot describe the dynamics, the hybrid semiclassical method based on the full scattering matrix gives excellent agreement with the first-principles TEBD simulation.

I. INTRODUCTION

Understanding nonequilibrium dynamics in interacting quantum many-body systems is one of the major challenges in today's statistical physics [1–4]. The formation of current-carrying steady states [5–8], the details of the thermalization process [9,10], entropy production [11–15], or the interplay with disorder [16–20] and topology [21–24] are just a few examples of the intriguing open questions which, due to recent breakthroughs in quantum simulation, can now be investigated experimentally.

While experimental results are abounding [25–30], available theoretical tools are quite limited in number and power. One-dimensional systems represent in this regard an exception and a theoretical testing ground for all methods and investigations, especially since in one dimension powerful analytical and numerical methods such as Bethe Ansatz [31], bosonization [32,33], density matrix renormalization group (DMRG) [34,35] exist to study equilibrium properties in detail. These methods can be extended to nonequilibrium steady states (NESSs) [36,37], while dynamics under nonequilibrium conditions can be efficiently simulated by the time-dependent DMRG [38] and the time-evolving block decimation (TEBD) algorithms [39]. However, in dynamical simulations, "exactness" or precision is typically lost after relatively short times due to the rapidly increasing entanglement of the state.

Recently, a semi-semiclassical approach (SSA) has been proposed to study generic, gapped one-dimensional quantum systems at *longer* times and small quasiparticle densities (i.e., small or slow quenches), and demonstrated on the sine–Gordon model [40]. As a generalization of the original semiclassical approach of Sachdev, Young, and Damle [41,42], the semi-semiclassical method treats trajectories of quasiparticles classically, but it accounts for the precise quantum evolution of the internal degrees of freedom fully quantum mechanically, and allows one to capture the associated quantum entanglement generation as well as simultaneous probabilistic processes. Though approximate, the SSA method is versatile, conceptually simple, and has also been extended to study dynamics in NESSs within the nonlinear sigma model [43].

Here we investigate quasiparticle creation and spin propagation after a quantum quench within the Haldane-gapped phase of the the antiferromagnetic spin-1 Heisenberg chain and compare the predictions of the semi-semiclassical method with TEBD simulations in detail. In particular, we consider the $S = 1$ Haldane chain with a time-dependent biquadratic interaction $J_2(t)$:

$$\hat{H}(t) = \sum_i J_1 \, \vec{S}_i \cdot \vec{S}_{i+1} + J_2(t)(\vec{S}_i \cdot \vec{S}_{i+1})^2 . \qquad (1)$$

Here $J_2(t) = J_2 \gamma(t)$, and the function $\gamma(t)$ changes from 1 to 0 around $t = 0$. We start from the ground state of $H(-\infty)$ and perform infinite volume TEBD (iTEBD) simulations [39] to obtain the full time-dependent wave function of the chain, $|\psi(t)\rangle$. To reach sufficiently long times comparable with the quasiparticle collision times, we need to exploit non-Abelian symmetries in our simulations. Using TEBD with non-Abelian symmetries enables us to reach times as large as $t \sim 10 \times J_1^{-1}$ for sudden quenches, where already clear signatures of quasiparticle collisions can be observed.

The quench protocol described above generates a gas of (entangled pairs of) quasiparticles in the final state. Cutting the infinite chain into two at time t and then measuring the
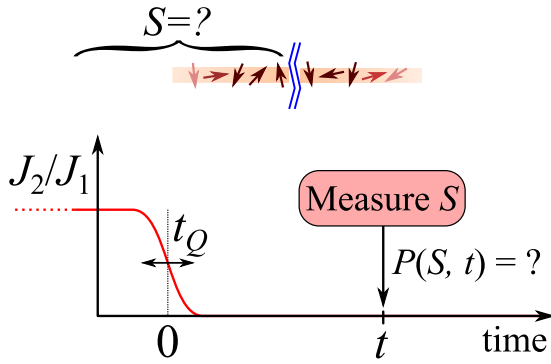
FIG. 1. Visualization of the quench protocol. The biquadratic coupling J_2 is turned off at $t = 0$ within a switching time t_Q. Later, at time t, the system is cut in two parts and the total spin S of the left part is measured. The statistics of the measurement is described by the spin distribution $P(S, t)$.

spin distribution on one side, $P(S, t)$, we can explore the propagation and collision of these quasiparticles (Fig. 1 and Fig. 2). We can, in particular, compute $P(S, t)$ in terms of the SSA and compare it to the results of TEBD simulations to find an astonishing agreement. As we shall also demonstrate, a theory based on completely reflective quasiparticle collisions [42,44–47] is not able to account for the observed behavior, and the full SSA is needed to get agreement with TEBD computations.

The paper is structured as follows. In Sec. II, we overview the basics of the microscopic non-Abelian iTEBD simulations and the SSA method. In Sec. III, the short-time ballistic behavior after the quench is analyzed. Then, in Sec. IV, we discuss the collision dominated regime of the dynamics. In Sec. V, we develop a perturbative quench theory and test its scope of validity. Our conclusions are summarized in Sec. VI.
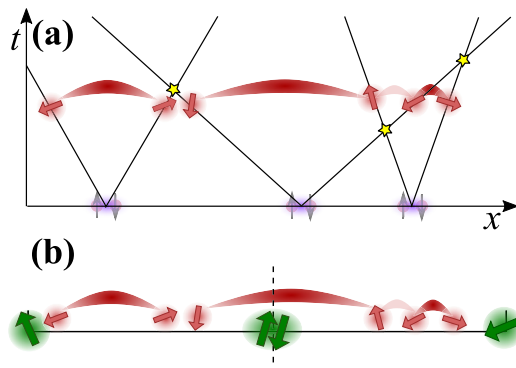

FIG. 2. The semiclassical quasiparticle picture. (a) World lines of the excited quasiparticle pairs. Entanglement structure of the gas is indicated by arched red stripes. At $t = 0$, singlet pairs with zero total momentum are excited. After the quench, the quasiparticles collide with each other; the scattering events are denoted by stars. (b) Visualization of the spin structure if the system is cut in two parts. The topological edge spins are denoted by large green arrows, while the quasiparticle spins are denoted by small red arrows. At the cut, the two "virtual" edge spins form a singlet. The total spin of the left part contains contributions of the edge spins, the quasiparticles, and vacuum fluctuations.

II. BASIC CONCEPTS AND NUMERICAL METHODS

Before presenting the main results, let us shortly review the two methods used to investigate the quench dynamics.

A. Non-Abelian TEBD lattice simulations

Here we discuss our non-Abelian TEBD algorithm only briefly, since our flexible and general way of treating non-Abelian symmetries in matrix product state (MPS) simulations will be presented in a separate publication [48].

The postquench dynamics of the system is described by the microscopic many-body Schrödinger equation,

$$i\partial_t |\Psi(t)\rangle = \hat{H}(t)|\Psi(t)\rangle, \quad (2)$$

which we solve numerically by means of the infinite chain time-evolving block decimation (iTEBD) algorithm [39]. The TEBD algorithm describes the real-time dynamics of the system based on the MPS description of the quantum state $|\Psi(t)\rangle$ [35,49],

$$|\Psi\rangle = \sum_{\{\sigma_l\}} \left(\dots M_{\sigma_{l-1}}^{[l-1]} M_{\sigma_l}^{[l]} \dots \right) |\{\sigma_l\}\rangle, \quad (3)$$

where the $|\sigma_l\rangle$ with $\sigma_l = \{0, +, -\}$ refer to the three quantum states of spin S_l at site l.

The MPS factorization of the quantum state $|\Psi\rangle$ relies on Schmidt decomposition [50]. Let us now focus on the case where $|\Psi\rangle$ is a spin singlet, and cut the chain into two halves between sites l and $l + 1$, i.e., treat the Hilbert space of the full chain as the product of its left and right halves. The Schmidt decomposition of $|\Psi\rangle$ then reads as [51,52]

$$|\Psi\rangle = \sum_{t_l} \frac{\Lambda_{t_l}^{[l]}}{\sqrt{2J_{t_l} + 1}} \sum_{m_l = -J_{t_l}}^{J_{t_l}} |t_l, m_l\rangle_{\text{left}} |t_l, \overline{m}_l\rangle_{\text{right}}, \quad (4)$$

where $|t_l, m_l\rangle_{\text{left}}$ and $|t_l, \overline{m}_l\rangle_{\text{right}}$ are the so-called Schmidt pairs [53]. Here t_l labels multiplets, while m_l refers to internal states within this multiplet having a total spin J_{t_l}. The values $\Lambda_{t_l}^{[l]}/\sqrt{2J_{t_l} + 1} > 0$ are the so-called Schmidt values and are independent of the internal label m_l.

The non-Abelian MPS (NA-MPS) representation of $|\Psi\rangle$ can be constructed by relating neighboring left Schmidt states while moving the cut position forward by one site:

$$|t_l, m_l\rangle_{\text{left}} = \sum_{t_{l-1}, \eta_l} A_{t_{l-1} \eta_l}^{[l] t_l} \sum_{m_{l-1}, \sigma_l} C_{m_{l-1} \sigma_l}^{m_l \eta_l}$$

$$\times |t_{l-1}, m_{l-1}\rangle_{\text{left}} |\sigma_l\rangle. \quad (5)$$

Here the tensor $C_{m_{l-1} \sigma_l}^{m_l \eta_l}$ contains the Clebsch–Gordan coefficients $\langle J_{t_{l-1}}, m_{l-1}; S_l, \sigma_l | J_{t_l}, m_l \rangle$, while the superindex $\eta_l \rightarrow \{J_{t_{l-1}}, S_l, J_{t_l}\}$ runs over allowed values of the three spins [54]. An iterative application of Eq. (5) yields the non-Abelian MPS (NA-MPS) representation Eq. (3) with

$$\left(M_{\sigma_l}^{[l]}\right)_{t_{l-1}, m_{l-1}}^{t_l, m_l} = \sum_{\eta_l} (A^{[l]})_{t_{l-1} \eta_l}^{t_l} C_{m_{l-1} \sigma_l}^{m_l \eta_l}, \quad (6)$$

corresponding to the two-layer NA-MPS structure sketched in Fig. 3. The tensors $A^{[l]}$ describe the transformation at the level of multiplets, and the contraction of the index η_l between $A^{[l]}$ and C ensures that the values of the three representation indices in the two tensors match.

The upper layer of the tensors $A^{[l]}$ contains all important physical information on the state $|\Psi\rangle$ and our TEBD time-evolver operators act only on this upper NA-MPS layer (see Appendix A). In other words, all expensive contractions within the Clebsch–Gordan layer are eliminated.

Here we use the infinite-chain TEBD algorithm that applies for translation invariant states [39]. In this case, both the tensors $A^{[l]}$ and the Schmidt values $\Lambda_{t_l}^{[l]}$ are independent of the site index l. Numerically, this one site translation invariance is, however, lowered to a two-site translation invariance due to the Suzuki–Trotter time evolution scheme [55,56], i.e., the tensors on the even and odd sublattices are slightly different.

The TEBD simulation provides the time-dependent tensors $A(t)_{t_{l-1}\, \eta_l}^{t_l}$ and the Schmidt values $\Lambda(t)_{t_l}$ (for details, see Appendix A). The distribution of the total spin of the half chain is then simply related to the Schmidt values:

$$P(S,t) = \sum_{t_l \mid J_{t_l} = S} |\Lambda(t)_{t_l}|^2 \,. \tag{7}$$

As shown in later sections, this distribution contains the essential information on the spin structure and spin entanglement of excited quasiparticles in the postquench state.

B. The semi-semiclassical approach

The numerical resources required for TEBD grow exponentially in time, and make the microscopic simulations tractable only for short times. However, the single-site-resolved knowledge of the quantum state is not necessary for answering many questions. The model Eq. (1) is known to be gapped [57,58], and its low-energy excitations are $S = 1$ triplet quasiparticles [58] described by the $O(3)$ nonlinear sigma model, an integrable relativistic field theory. Low energy quasiparticles therefore have a (close to) relativistic dispersion,

$$\omega_q = \sqrt{\Delta^2 + c^2 q^2} \,, \tag{8}$$

where the gap and the "speed of light" are given in terms of the microscopic parameters of the Hamiltonian as [58]

$$\Delta \approx 0.4105\, J_1 \,, \quad c \approx 2.472\, J_1 a \,. \tag{9}$$

The finite gap ensures that, in the case of small quenches, the postquench state is a dilute gas of quasiparticles.

From the locality and the translation invariance of the Hamiltonian, we can also conclude that shortly after the quench the state consists of spatially localized uncorrelated quasiparticle pairs. Moreover, since the quench protocol conserves SU(2), these quasiparticle pairs must form SU(2) singlets. These assumptions form the basis of the semi-semiclassical approximation [40], where the quasiparticles' spatial degrees of freedom are treated classically in a Monte Carlo sampling of the possible world-line configurations, while their internal spin states are are constructed as an NA-MPS state, and followed at the quantum level. As sketched in Fig. 2, the evolution of the quasiparticle spin states can be described by consecutive application of the two-particle S-matrix at collision events—if the gas is dilute enough.

The condition for the applicability of semiclassical approach is that the mean interparticle distance must be larger
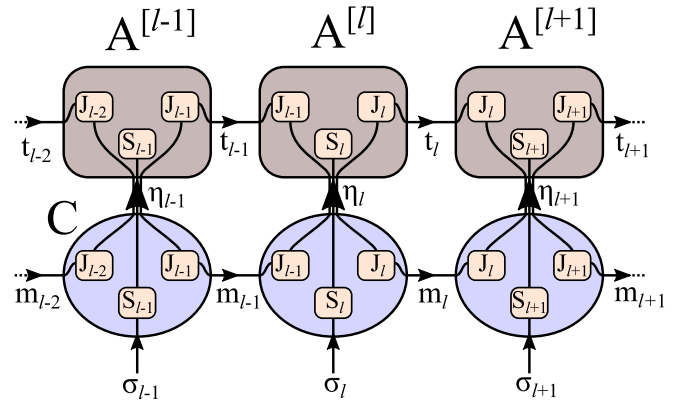

FIG. 3. Two layer structure of the SU(2) invariant non-Abelian matrix product state. The lower layer contains the Clebsch–Gordan coefficients and is unaffected by time evolution. Representation indices are shown as bubbles within the tensors: These indices indicate the sparse block structure of these tensors.

than the Compton wavelength of the particles [59]:

$$\rho^{-1} > c/\Delta \,. \tag{10}$$

As we shall see, this condition is satisfied even for relatively large quenches in our model.

This semi-semiclassical formalism allows us to compute the time-dependent spin distribution of a half chain, $P(S,t)$. Half-chain spin fluctuations have two sources in the SSA: (1) cutting the vacuum state of an infinite Haldane chain into two gives rise to a non-trivial spin distribution, $P_0(S_0)$, and (2) quench generated quasiparticles carry spins (and entanglement) across the cut.

To determine the first contribution, we first constructed the postquench ground state with $J_2 = 0$ using TEBD, cut it into two, and determined $P_0(S_0)$ from the Schmidt values. As shown in Table I, we clearly observe the presence of two topologically protected spin-1/2 end spins after the cut [60,61]: These yield a triplet state with almost 74% probability and a singlet state with more than 24% likelihood.

This can be understood as follows: constructing the density operator of a half chain from the ground-state configuration of the infinite chain corresponds to cutting suddenly the infinite chain into two half chains, i.e., a sudden quench. Before the cut, the ground state is a singlet and the two topologically protected spin $-1/2$ end spins also form a singlet. Would we separate *slowly* (but not infinitely slowly) the chain into two

TABLE I. Left: Ground-state spin structure of a semi-infinite spin-1 Haldane chain. Right: Slopes of the probability distributions at short times, $r_S = \mathrm{d}P(S,t)/\mathrm{d}t|_{t=0}$, as predicted by the semiclassical theory, and as extracted from the TEBD simulations for quench duration $t_Q = 1.6/J_1$.

S_0	$P_0(S_0)$	S	$(r_S/r_0)_{\mathrm{SC}}$	$(r_S/r_0)_{\mathrm{TEBD}}$
0	0.2426	0	1	1
1	0.7388	1	1.535	1.549(22)
2	0.0186	2	−2.481	−2.502(20)
		3	−0.054	−0.0572(9)

half chains at the center, we would create another singlet pair of end spins at the cut. Since the end spins at $\pm\infty$ and the ones at the cut are independent, this implies that the topologically protected half spins of the resulting semi-infinite chain will be independent, and thus form a triplet with probability 3/4 and and a singlet with probability 1/4. Performing a sudden cut slightly changes this picture, since it generates with a small probability quasiparticles across the cut. The latter alter the total spin of the half chain, although the probability of these processes is around $\sim$2% according to our numerical results.

Semi-semiclassics can be used to determine the second contribution, that of pairs of quasiparticles created by the J_2 quench. This gives rise to the quasiparticles' spin distribution, $P_{qp}(S_{qp})$. Assuming that the spin orientation of the quasiparticles is independent of those of the vacuum fluctuations, we obtain the total half-chain spin distribution [62]:

$$P(S, t) = \sum_{S_0} \sum_{S_{qp}} \delta_{S \in S_0 \otimes S_{qp}} (2S+1) \frac{P_0(S_0)}{2S_0 + 1} \frac{P_{qp}(S_{qp}; t)}{2S_{qp} + 1} . \tag{11}$$

The distribution $P_{qp}(S_{qp})$ can, in general, be determined only numerically. However, as described in the next two sections, we have simple analytical expressions at very short times as well as in the limits of completely reflective and completely transmissive scatterings, valid for very cold and very hot gases of quasiparticles, respectively.

III. SHORT-TIME BALLISTIC BEHAVIOR

First we analyze the initial change of $P(S)$ shortly after the quench, where the quasiparticle picture gives simple predictions. As discussed before, the initial state is a superposition of states containing randomly localized spin-singlet quasiparticle pairs with random velocities $\pm v$ and a quasiparticle density ρ. The distribution of the magnitude of the velocity, $f(v)$, depends on the details of the quench. The total spin of the left half chain changes when the first $S = 1$ quasiparticle crosses the position of the cut and carries spin from one half to the other. The probability of this happening within time t is simply

$$Q(t) = \rho \int_0^c vt f(v) dv \equiv \frac{t}{2\tau} , \tag{12}$$

because the quasiparticle of velocity v can come from an interval of length $|v|t$ on either side, touching the cut, but it must move to the right direction. The collision time τ above is defined as the ratio of the mean interparticle spacing and the mean velocity.

For short times, we can neglect multiple crossings. After the first singlet pair has reached the cut position, the spin of the half chain changes from 0 to 1 (see Fig. 5), so in Eq. (11) we have

$$P_{qp}(S_{qp} = 1; t) = t/(2\tau) + \dots , \tag{13a}$$

$$P_{qp}(S_{qp} = 0; t) = 1 - t/(2\tau) + \dots , \tag{13b}$$
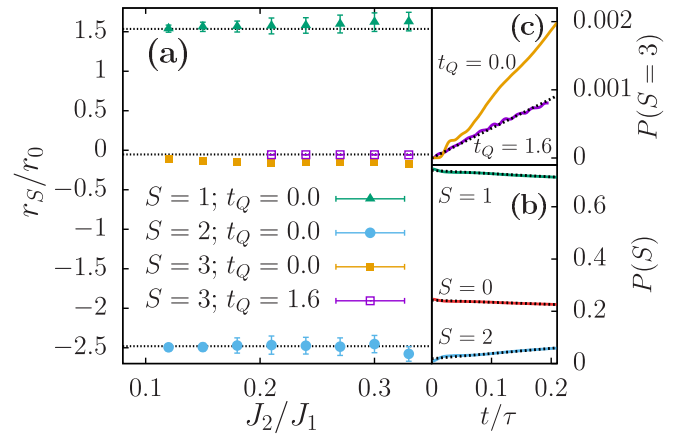

FIG. 4. (a) The initial relative rates r_S/r_0 extracted from the microscopic simulation of the Heisenberg chain as a function of the quench magnitude, J_2/J_1. Data for sudden quench are shown as symbols, while the dotted lines indicate the semi-semiclassical predictions. The relative rates for a smooth quench ($t_Q = 1.6/J_1$) are also plotted for $S = 3$ as empty squares. (b) Short-time behavior of the $P(S, t)$ spin distribution for sectors $S = \{0, 1, 2\}$ in the case of a sudden quench $J_2/J_1 = 0.12$. Dotted black lines show linear fits used to determine the initial rates. (c) Short-time behavior of $P(S = 3, t)$ for a sudden quench with $J_2/J_1 = 0.12$ and a smooth quench with $t_Q = 1.6/J_1$ and $J_2/J_1 = 0.33$.

and we find

$$P(0, t) = P_0(0) - \left(P_0(0) - \frac{P_0(1)}{9} \right) \frac{t}{2\tau} + \dots ,$$

$$P(S, t) = P_0(S) + \frac{2S+1}{6}$$
$$\times \left(\frac{P_0(S-1)}{2S-1} - \frac{2 P_0(S)}{2S+1} + \frac{P_0(S+1)}{2S+3} \right) \frac{t}{\tau} + \dots . \tag{14}$$

Using the vacuum spin probabilities in Table I, we can compute, independently of $f(v)$, the ratios of the slopes $r_S = \frac{dP(S,t)}{dt}\big|_{t=0}$ of the initial linear time dependencies with the result shown in Table I.

We have confronted these predictions with microscopic TEBD simulations, shown in Fig. 4. The short-time $P(S, t)$ functions are plotted for $S = 0, 1, 2$ in Fig. 4(b) as functions of time for a representative sudden quench. The relative rates r_S/r_0 extracted from these and similar curves obtained with various quench sizes are displayed in the Fig. 4(a). In accordance with the quasiparticle picture, the relative rates are independent of the quench size. The agreement with the quasiparticle prediction is excellent for $S = 0, 1, 2$, while there is a small deviation for sudden quenches for $S = 3$. The latter can be attributed to the difficulty of extracting the universal initial rate due to transient oscillations (cf. upper curve in Fig. 4(c), comparing the results for a sudden and a finite time quench for $S = 3$). The oscillations are not present for smooth finite time quenches, and for these we get excellent agreement with the semiclassical prediction. This agreement between the prediction of the quasiparticle picture and the numerics gives strong evidence that the quasiparticle picture
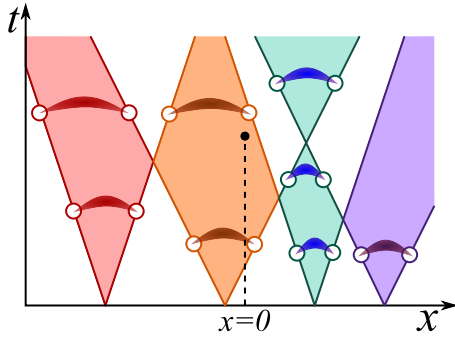
FIG. 5. Visualization of quasiparticle spin dynamics in the fully reflective limit. Initially the pairs form singlet pairs, indicated by colored shading. In this limit, singlet bonds between neighboring particles, indicated by arcs, remain intact.

is correct. In the following sections, we test the validity of the semiclassical description at longer times.

IV. COLLISION DOMINATED REGIME

At later times after the quench, several particles can cross from one half chain to the other from both directions. Moreover, one has to take into account the effect of collisions. In this section, after considering two analytically tractable limiting cases, we apply the semi-semiclassical method and compare its results with the TEBD numerics.

A. Simple limits

Let us first consider two limits, those of completely reflective and completely transmissive collisions, in which we can compute the spin distribution function analytically.

1. Completely reflective limit

In the universal low-energy limit, the two-particle scattering matrix of gapped models with short range interaction is a permutation matrix, corresponding to perfect reflection of the incoming quasiparticles. This limiting S-matrix was used in early works [42,44–47] on the semiclassical method to describe the dynamics at low temperatures. The S-matrix for the $O(3)$ nonlinear sigma model, describing our spin Hamiltonian, is exactly known, and also describes perfectly reflective processes in the limit of small relative rapidities (see Appendix B).

The initial state consists of pairs of quasiparticles that form spin singlets, and in this reflective limit, neighboring quasiparticle pairs remain singlets even after many collisions (see Fig. 5). If we cut the system into two half chains, the quasiparticle contribution to the total spin of the left part at a given time is $S_{qp} = 0$ if the cut lies between pairs, while $S_{qp} = 1$ if the cut breaks a pair. It is easy to see that the first situation is realized if the number of quasiparticles crossing from one half to the other up to the given time is even, and the second if this number is odd. The crossing number can be computed using the straight lines in Fig. 5 (the would-be trajectories of noninteracting particles). The total number of crosses from the left and right, n_+ and n_-, follow independent
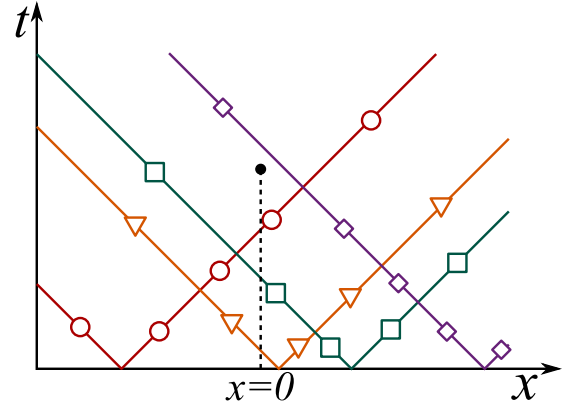

FIG. 6. Quasiparticle spins in the fully transmissive (ultrarelativistic) limit. Members of entangled quasiparticle pairs are marked by specific symbols on the worldlines. Interaction between quasiparticles is negligible in this limit: The particles simply cross each other without changing their spins.

Poisson distribution,

$$p(n_+, n_-) = \frac{1}{n_+! \, n_-!} q(t)^{n_+ + n_-} e^{-2q(t)} , \qquad (15)$$

where $q(t) = \frac{1}{2}\rho t \int_0^c dv \, v f(v) = Q(t)/2 = 1/(4\tau)$ is the probability that a trajectory crosses the cut from the left (or from the right). The probabilities of having even ($S_{qp} = 0$) or odd ($S_{qp} = 1$) number of crossings are then

$$
\begin{aligned}
P_{qp}^{refl}(S_{qp}, t) &= \sum_{n_+, n_- = 0}^{\infty} p(n_+, n_-) \frac{1 + (-1)^{S_{qp}}(-1)^{n_+ + n_-}}{2} \\
&= \frac{1}{2}(1 + (-1)^{S_{qp}} e^{-t/\tau}) . \qquad (16)
\end{aligned}
$$

Note that expanding for short time, we recover the expressions in Eqs. (13). Substituting the above result into Eq. (11) the total spin distribution can be computed in the totally reflective limit.

2. Completely transmissive (ultrarelativistic) limit

Very high-energy quasiparticles do not interact with each other. This can also be verified on the exact S-matrix of the nonlinear sigma model in Appendix B, in the limit of very large rapidity differences, i.e., of ultrarelativistic quasiparticles. In this limit, the original spin singlets remain singlets, but now the members of a pair keep moving away from each other following the light cone (see Fig. 6). Since quasiparticles crossing the cut are independent of each other, the quasiparticle spin distribution is given by

$$P_{qp}^{trans}(S_{qp}; t) = \sum_N P_{spin}(S_{qp}|N) \, P_{cross}(N; t) , \qquad (17)$$

where $P_{cross}(N; t) = \frac{Q(t)^N}{N!} e^{-Q(t)}$ is the Poisson probability distribution of the number of world lines that cross the cut from any side, while $P_{spin}(S|N) = (2S + 1)M_{S|N}/3^N$ is the distribution of the total spin of N particles with random spin orientations. Here $M_{S|N}$ counts the multiplets of spin S in the N-particle space, and it can be calculated iteratively from the
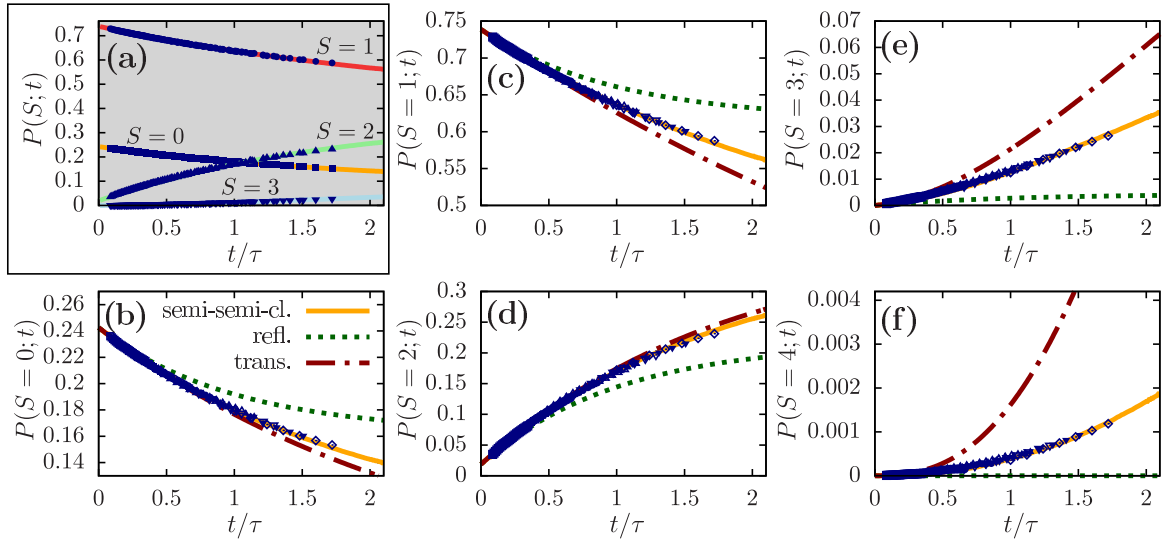
FIG. 7. Spin distribution after a sudden quench as a function of t/τ. Symbols are results of microscopic simulations on the Heisenberg chain for different values of the quench magnitude $J_2/J_1 \in [0.12, 0.36]$. The values of τ for different quench magnitudes were found by searching the best collapse of the curves. Panels (b)–(f) display the probabilities of each spin separately. The green dotted curves show the prediction in the fully reflective limit, while red dash-dotted lines show the fully transmissive values. The results of the microscopic simulation differ significantly from both limits, but are well described by the semi-semiclassical simulation performed using a cutoff parameter $E_0 = 4J_1$. Panel (a) shows the curves $P(S;t)$ for all spin sectors together. Here colored lines show the corresponding semi-semiclassical simulation.

recursion relation,

$$M_{S|N} = M_{S+1|N-1} + (1 - \delta_{S,0})(M_{S|N-1} + M_{S-1|N-1}), \quad (18)$$

with initial condition $M_{S|0} = \delta_{S,0}$. Solving these equations iteratively, we can quickly compute P_{qp}^{trans} at any time.

B. Hybrid semiclassical dynamics

In general, the scattering is neither fully reflective nor fully transmissive. The result of each collision is instead a superposition of possible outgoing states with respective amplitudes given by the scattering matrix. In the O(3) nonlinear sigma model, the total spin and also its z component are conserved in the scattering of the $S = 1$ quasiparticles, but transmissive and reflective processes as well as quasiparticle spin flips all occur with finite scattering amplitude. In the $S_T^z = 0$ scattering channel, for example, a superposition of transmissions and reflections occur for incoming particles $(+, -)$, but even the process $(+, -) \longrightarrow (0, 0)$ is allowed.

The two-body scattering matrix is exactly known for the O(3) nonlinear sigma model. In our hybrid semiclassical method, we use this S-matrix: Whenever there is a collision of quasiparticles, we act on the two colliding quasiparticle spins by the corresponding O(3) S-matrix. This goes beyond standard semiclassical treatments not only by allowing nontrivial scattering processes, but also by treating the spin part of the many-body wave function fully quantum mechanically [40]. Here the quantum state of the spin part—not including the topological end spins—is described by an NA-MPS, where the vertical, physical legs—in contrast to the microscopic simulations—stand for the quasiparticles' spins. For a given world-line configuration, the action of the S-matrices are taken into account by means of the TEBD algorithm [39,40]. The quasiparticle part of the spin fluctuations can be

calculated similarly to Eq. (7) for each world-line configuration, and the final $P_{qp}(S_{qp}, t)$ distribution can be determined by averaging over many world-line configurations.

Apart from the S-matrix, the other main input for the method is the momentum distribution of the quasiparticles, which is not easy to measure or calculate. In our simulation, we used the distribution

$$n(q) \propto \frac{q^2}{\sinh^2(\omega_q/2E_0)}, \quad (19)$$

with $\omega_q = \sqrt{\Delta^2 + q^2c^2}$ the quasiparticle dispersion relation and E_0 a tunable cutoff parameter. This particular functional form is motivated by the perturbative calculation outlined in Sec. V.

We compare the results of the semi-semiclassical method with the microscopic TEBD numerics for sudden quenches in Fig. 7. Different symbols correspond to quenches of different magnitude. In the SSA, the distribution of scattering matrices depends exclusively on the velocity distribution of quasiparticles, which is, in turn, determined exclusively by the microscopic quench protocol. In the perturbative limit, we expect this distribution to be independent of the amplitude of the quench. The amplitude of the quench is only supposed to influence the density of the quasiparticles created, and thus the collision time. Therefore, we expect that the functions $P(S, t)$ can be scaled on the top of each other by rescaling time.

This is indeed what we find by studying sudden quenches of different sizes, $J_2/J_1 \in [0.12, 0.36]$, for which the curves $P(S, t)$ collapse when plotted against t/τ (see Fig. 7). For smaller quenches, the collision time τ is determined from the early time slope of the functions in Eq. (14), while for larger quenches, where transient oscillations are superposed at early times, we just rescaled the curves to achieve the best collapse.
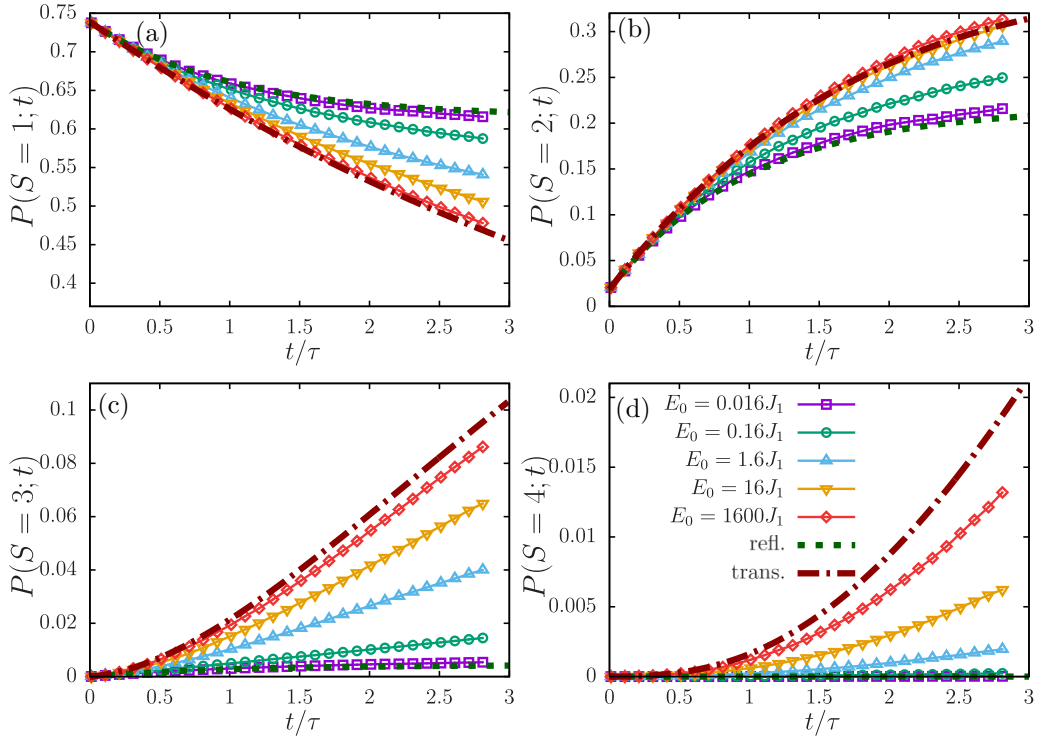
FIG. 8. Spin distribution in the semi-semiclassical simulation with different cutoff parameters. The dashed green lines show the fully reflective limit, while the red dash-dotted line shows the transmissive limit. The semi-semiclassical simulation results in spin distributions between these two limits, depending on the value of the cutoff. For small cutoff, the results are close to the reflective limit, while for large cutoff the transmissive limit is approached.

Remarkably, the same rescaling factor worked for all different spin values in each case.

The resulting curves can be compared to semiclassical predictions. The first observation is that neither of the special limits can reproduce the results of the microscopic numerical simulation [cf. green dotted and red dash-dotted curves in Figs. 7(b)–7(f)]. In particular, the standard semiclassical method based on totally reflective collisions cannot account for the postquench dynamics, and the numerically determined time evolution lies between the predictions of completely reflective and completely transmissive computations.

Remarkably, however, the semi-semiclassical results give excellent agreement with the TEBD data. We recall that there is a single free parameter in the semiclassical calculation, the cutoff parameter E_0. The same choice, $E_0 = 4J_1$, gave the best agreement for all spin values S. This cutoff is close to the quasiparticles' bandwidth [58].

The effect of the cutoff on the semi-semiclassical spin distributions for $S = 1, \ldots, 4$ is illustrated in Fig. 8. A very small cutoff leads to slow quasiparticles with predominantly reflective scattering, and dynamics close to the standard semiclassical prediction of Sec. IV A. For large cutoffs, on the other hand, the majority of the quasiparticles is ultrarelativistic and collide mostly by transmissive scattering. Varying E_0, the SSA interpolates between these two limiting cases.

V. PERTURBATIVE QUENCH THEORY

In this section, we develop a perturbative description of the quench in terms of an effective field theory and compare its

implications with the results of our TEBD simulations and the semi-semiclassical interpretation thereof. Certain details of the derivations are given in Appendix C.

Our first step is to replace the original Hamiltonian Eq. (1) by a phenomenological quasiparticle Hamiltonian, and to express the postquench Hamiltonian as

$$\hat{H}_0 = \sum_{q,\sigma} \omega_q \, b^\dagger_{q,\sigma} b_{q,\sigma} \, . \qquad (20)$$

Here the operators $b^\dagger_{q,\sigma}$ create quasiparticles of momentum q, energy ω_q, and spin $\sigma = \pm 1, 0$. As discussed earlier, switching off J_2 creates singlet pairs of quasiparticles with opposite momenta. This is implemented within our effective field theory by the term [63]

$$\hat{H} = \sum_{q,\sigma} \left\{ \omega_q(t) b^\dagger_{q,\sigma} b_{q,\sigma} + \frac{1}{2} g_q(t) (-1)^\sigma \right. $$
$$\left. \times \, (b^\dagger_{q,\sigma} b^\dagger_{-q,-\sigma} + b_{q,\sigma} b_{-q,-\sigma}) \right\}, \qquad (21)$$

with the time-dependent dispersion and pair creation amplitudes

$$\omega_q(t) = \omega_q + J_2 \lambda(t) \, \Delta_q \, , \quad g_q(t) = J_2 \lambda(t) \, g_q . \qquad (22)$$

Here $\lambda(t)$ describes the time-dependent profile of the quench with $\lambda(t \to -\infty) = 1$ and $\lambda(t \to \infty) = 0$. The precise momentum dependence of the couplings Δ_q and g_q depends on microscopic details of the Hamiltonian $\hat{H}_0$ and the perturbing quench operator. At leading order in perturbation theory, the

momentum distribution of quasiparticles is determined by the quasiparticle dispersion ω_q, the specific form of $\lambda(t)$, and by the pair creation amplitude, g_q. This latter typically vanishes in the limit $q \to 0$ linearly, reflecting the fact that low-energy quasiparticles behave as hard-core bosons.

Being quadratic, the simple model outlined above can be treated analytically, and can be used to determine the momentum distribution of the quasiparticles analytically. For small and smooth quenches we find

$$n(q) \propto |g_q|^2 \, \frac{J_2^2}{\omega_q^2} \, \left| \frac{\widetilde{\mathrm{d}\lambda}}{\mathrm{d}t}(2\omega_q) \right|^2 , \qquad (23)$$

where the tilde denotes the Fourier transform. Note that $\lambda(t)$ does not depend on the amplitude of the quench, only on its duration and shape. Quite naturally, the quasiparticle density is proportional to the squared magnitude of the quench. Consequently, the collision rate $1/\tau$ defined in Eq. (12) is also just proportional to J_2^2.

This prediction is checked in Fig. 9(a), where we plot the inverse collision times extracted from TEBD as functions of J_2/J_1 for three different quench speeds. The quadratic dependence is valid up to $J_2/J_1 \approx 1/3$ which is just the so-called AKLT point [60], suggesting that perturbation theory holds for quenches even up to this size. Also, slower, more adiabatic quenches create less quasiparticles, reflected in a lower collision rate.

As the quench magnitude J_2 only appears in the prefactor in Eq. (23), the normalized velocity distribution is predicted to be independent of it in this perturbative regime. The energy density should therefore be proportional to the quasiparticle density with a proportionality factor depending on the shape of $\lambda(t)$. As a consequence, the product of the collision time and the energy density ρ_e should be independent of the size of the quench if perturbation theory holds. This prediction is tested in Fig. 9(b), where we plot the product $\rho_e \tau$ against J_2/J_1 for various quench durations. Here the quasiparticle energy density was measured in the TEBD simulation by taking the difference of the postquench and the vacuum energy densities. It can be seen that the product is indeed approximately constant up to $J_2/J_1 \approx 1/3$, i.e., in the domain of perturbation theory identified above.

To make a more quantitative comparison between TEBD and our semiclassical method, we specify the shape of the quench as

$$\lambda(t) = \tfrac{1}{2}[1 - \tanh(t/t_Q)]. \qquad (24)$$

We furthermore assume a simple linear dependence of g_q around $q = 0$ (see Appendix C) and use a relativistic dispersion relation ω_q with the microscopic parameters given in Eqs. (9). With these approximations, we obtain the quasiparticle momentum distribution used in our semi-semiclassical simulations, Eq. (19) with $E_0 = t_Q$:

$$n(q) \propto J_2^2 \frac{q^2}{\sinh^2(\pi t_Q \omega_q)} . \qquad (25)$$

With this distribution, we can compute the product of the energy density and the collision time for different quench durations t_Q. The results are shown in Fig. 10 together with the TEBD data for quenches with $J_2/J_1 = 0.24$. There is a
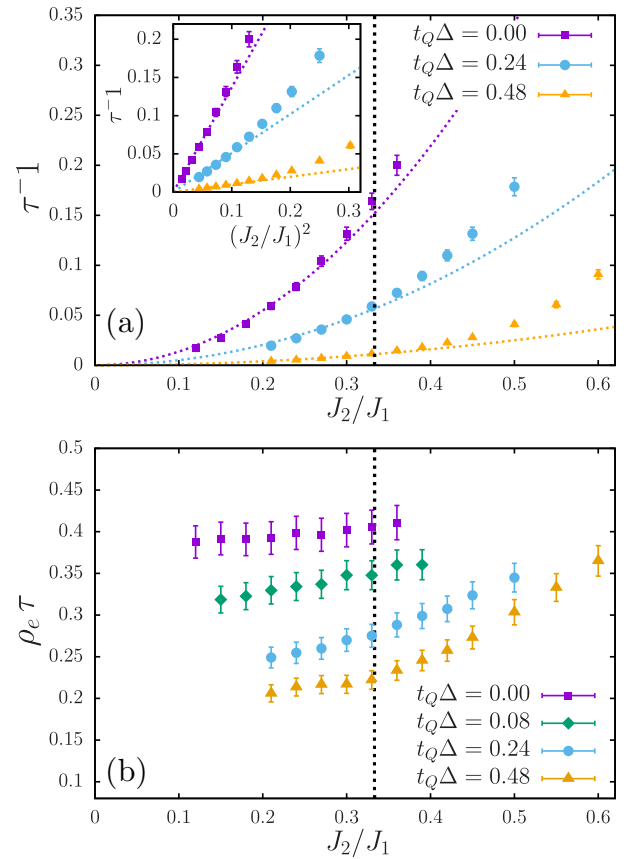

FIG. 9. Checking basic predictions of perturbation theory. Different symbols show data for different quench times t_Q. (a) The fitted inverse collision time τ^{-1} as a function of the quench magnitude J_2/J_1. The vertical dashed line indicates the AKLT point, $J_2/J_1 = 1/3$. Perturbation theory predicts quadratic dependence of τ^{-1} on J_2/J_1 that seems to be valid up to the AKLT point. The inset shows the same data but with quadratic scale on the horizontal axis. (b) The product of the energy density ρ_e and the collision time τ as a function of the quench magnitude J_2/J_1. Perturbation theory predicts this value to be constant for a given value of T_Q, which seems to hold up to the AKLT point. The error bars arise from the uncertainty of the fitted value of τ, while the relative error of the measured energy density is small.

reasonable agreement for not very fast quenches. This demonstrates convincingly that the semiclassical picture based on relativistic quasiparticles with perturbatively computed momentum distribution provides a valid qualitative and quantitative description of the postquench dynamics.

Let us close this section by verifying the consistency condition Eq. (10) of the SSA. Even though we cannot measure the particle density directly, we can set an upper bound on it using the energy density:

$$\rho \lesssim \rho_e/\Delta . \qquad (26)$$

This implies that the semiclassical condition Eq. (10) is certainly satisfied if

$$c\rho_e < \Delta^2 \qquad (27)$$

holds. We checked that this inequality was always satisfied in our simulations, except for the largest sudden quench with
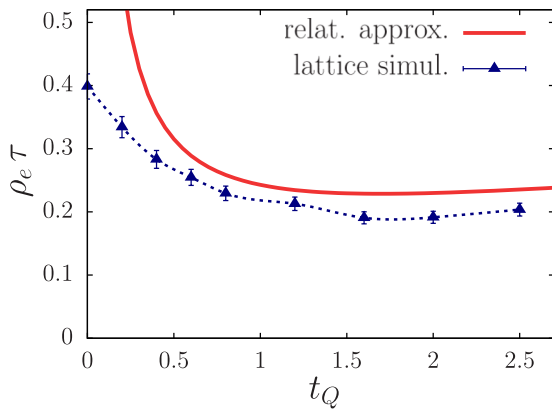
FIG. 10. The product of the energy density ρ_e and the collision time τ as a function of the quench time t_Q for $J_2/J_1 = 0.24$. The continuous red line shows the prediction of the relativistic minimal model. While the simple prediction largely fails for small quench times t_Q, for larger t_Q the agreement is reasonable.

$J_2/J_1 = 0.36$, where $c\rho_E/\Delta^2 \approx 1.2$ was found. However, for sudden quenches Eq. (26) strongly overestimates the particle density, i.e., Eq. (10) is expected to be valid even in this largest sudden quench.

VI. SUMMARY

In this paper, we have studied numerically the statistics of spin transfer after a quantum quench in the Haldane chain, and compared it with the predictions of the SSA, developed in Ref. [40]. As we demonstrate, the probability distribution $P(S, t)$ of transferred spins, extracted from non-Abelian TEBD quench simulations, contains a surprising amount of information: In addition to detecting the presence of topologically protected end states [60,61], it gives insight to the internal spin structure and velocity distribution of quasiparticles as well as to the nature of their collisions.

Application of SU(2) symmetries allows us to reach sufficiently large bond dimensions in the range of 2000 multiplets corresponding to 10 000 states [48], and to reach long enough simulation times to overlap with the range of validity of semi-semiclassics, and to observe effects related to quasiparticle collisions. We find that spin distributions, as computed through our full TEBD simulations, are in perfect agreement with those determined from the SSA: The short-time behavior of $P(S, t)$ reveals the presence of spin $S = 1$ quasiparticles traveling ballistically, while at longer times we enter a collision-dominated regime, where collisions are neither reflective [42,45–47] nor transmissive [64]. In this regime, it appears to be absolutely necessary to incorporate the coherent time evolution of the spin wave function, and to follow its quantum mechanical evolution, as performed by the hybrid SSA.

For a sudden quench, the functions $P(S, t)$ are found to be universal functions of t/τ, with τ the collision time. This universal scaling can also be simply explained within the semi-semiclassical theory: the size of the quantum quench has a direct influence on the quasiparticle density, $\varrho \sim J_2^2$, and thus the scattering rate, $1/\tau \sim \rho$, however, it does not change the velocity distribution of the quasiparticles and the structure

and distribution of scattering matrices. Therefore, the statistics of collisions and the statistical time evolution of the wave function is independent of the size of the quench if time is measured in units of collision time.

The precise velocity distribution does depend, however, on details of the quench protocol and the quench time t_Q. Correspondingly, for finite time quenches, we observe an explicit dependence of the functions $P(S, t)$ on the quench time (quench protocol). This explicit dependence is very well captured by simply changing the energy cutoff of the quasiparticles' velocity distribution, $E_0 \sim 1/t_Q$. This latter correspondence, and the velocity distributions used in our semi-semiclassical simulations, have both been motivated by a perturbative field theoretical quantum quench theory, presented in Sec. V.

The extension of perturbative quench regime as well as the range of validity of our SSA appear to be astonishingly large. First, $1/\tau$, directly proportional to the density of quasiparticles is found to scale as $\sim J_2^2$ up to quench sizes of $J_2/J_1 \approx 0.3$, a value very close to the AKLT point at $J_2/J_1 = 1/3$. Second, our assumption of a quench-size independent velocity distribution is also verified by direct measurements of the quasiparticles' energy density on the Haldane chain. Also quite remarkably, our perturbative field theoretical calculation assuming a simple relativistic quasiparticle spectrum yields a *quantitative* estimate for the dimensionless energy density $\rho_e\tau \sim \rho_e/\rho$, in very good agreement with our full TEBD spin chain simulations for quench times $t_Q \gtrsim 0.5/J_1$. This is, again, quite astonishing, since sudden quenches generate many quasiparticles presumably outside the regime of our effective field theory. Apparently, however, quasiparticles close to the gap appear to play the dominant role in the spin transport studied here.

In our semi-semiclassical simulations, we have used the S-matrix of the O(3) nonlinear sigma model, an integrable field theory describing the large distance behavior of the Haldane chain. This approximation is not entirely necessary: In principle, one can determine the exact S-matrix from MPS simulations [65,66], and we could have used the exact S-matrix of the $S = 1$ Heisenberg chain [66], extracted from DMRG simulations, and thereby incorporate effects associated with irrelevant operators. However, although we expect this approximation to become inappropriate at very long times [6,10], we could not see any sign of this breakdown even for the largest timescales we could reach with our TEBD simulations, $t \sim 10 \times J_1^{-1}$.

The calculations presented here have thus two general conclusions: On the one hand, they show that semi-semiclassical calculations are simple (although not entirely controlled) methods, which are able to capture important features of nonequilibrium quantum dynamics at timescales much above the microscopic time scales. On the other hand, our studies reveal the power and richness of full counting statistics and full distributions, such as $P(S, t)$, containing precious information on correlations, equilibration and dynamics [67–72].

APPENDIX A: NA-TEBD

The MPS-based calculations of the time evolution—both the microscopic simulations of the $S = 1$ chain and the hybrid semi-semiclassical simulations—were performed by a variant of the standard TEBD algorithm [39] that exploits the presence of the non-Abelian SU(2) symmetry; we call our variant of the algorithm NA-TEBD, and our code is similar to the approaches described in Refs. [52,73–75], but by the introduction of the η-legs the generalization to other non-Abelian symmetries becomes easier [48,54].

In the TEBD algorithm, the time evolution of the MPS wave function is simulated by consecutive application of two-site unitary evolvers [39], based on the Trotter–Suzuki decomposition [55,56]. Considering now the SU(2) symmetric case, the evolvers like $U^{\sigma_l \sigma_{l+1}}_{\sigma'_l \sigma'_{l+1}}$, acting on the neighboring sites l and $l + 1$, preserve the SU(2) symmetry, and one naturally would like to exploit this property. Formally, one should contract the legs σ_l, σ_{l+1} of the tensor U with the ones of the Clebsch–Gordan tensors in the two-layer NA-MPS (see Figs. 3 and 11). However, if the SU(2) symmetry is preserved by the two-site evolver, then after the application of it, the Clebsch-layer of the NA-MPS should remain the same, i.e., only the tensors $A^{[l]}$ and $A^{[l+1]}$ change. Using the standard orthogonality relations of the Clebsch–Gordan coefficients, we can determine the "symmetric" version of the two-site evolver that can be directly applied on the legs η_l and η_{l+1} of the tensors $A^{[l]}$ and $A^{[l+1]}$. This "symmetric" evolver is defined as [see also Fig. 11(a)]

$$[U_{\text{sym}}]^{\eta_l \eta_{l+1}}_{\eta'_l \eta'_{l+1}} = \sum_{\substack{m_{l-1} \\ m_l \\ m'_l \\ m_{l+1}}} \sum_{\substack{\sigma_l \\ \sigma_{l+1} \\ \sigma'_l \\ \sigma'_{l+1}}} \frac{1}{2J_{l+1}+1} U^{\sigma_l \sigma_{l+1}}_{\sigma'_l \sigma'_{l+1}}$$

$$\times\, C^{m_l\, \eta_l}_{m_{l-1}\, \sigma_l} C^{m_{l+1}\, \eta_{l+1}}_{m_l\, \sigma_{l+1}} \left(C^{m'_l\, \eta'_l}_{m_{l-1}\, \sigma'_l}\right)^* \left(C^{m_{l+1}\, \eta'_{l+1}}_{m'_l\, \sigma'_{l+1}}\right)^*. \tag{A1}$$

The resulting tensor can be determined and stored before the simulation procedure, and later can be directly applied on the upper layer of the NA-MPS. It is important to remark that the blocks of the resulting tensor $[U_{\text{sym}}]^{\eta_l \eta_{l+1}}_{\eta'_l \eta'_{l+1}}$ are specified by eight irreducible representation ("total spin") indices that are $\{J_{l-1}, S_l, J_l, S_{l+1}, J_{l+1}, S'_l, J'_l, S'_{l+1}\}$.

After the determination of U_{sym}, the standard TEBD algorithm as described in Ref. [39] can be used to evolve the upper layer of the NA-MPS without any relevant modification as shown in Fig. 11(b). In other words, the layer of
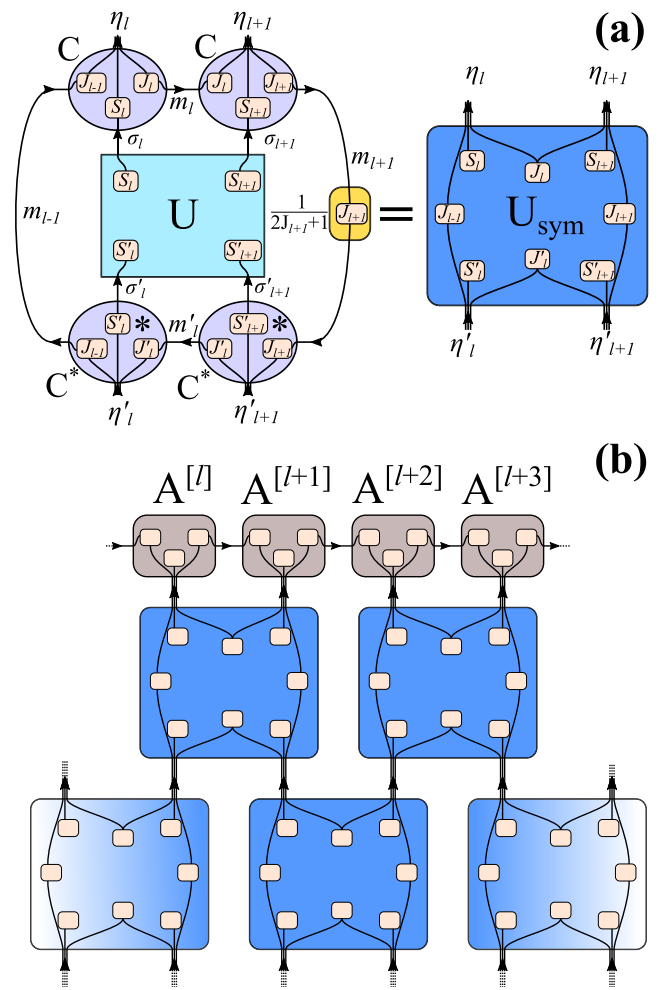
FIG. 11. (a) Graphical representation of the defining Eq. (A1). The blocks of the resulting $[U_{\text{sym}}]^{\eta_l \eta_{l+1}}_{\eta'_l \eta'_{l+1}}$ tensor are specified by eight irreducible representation indices. (b) The NA-TEBD algorithm. The symmetric evolvers U_{sym} are directly applied on the upper layer of the NA-MPS.

Clebsch–Gordan coefficients does not appear during the simulations, making our NA-TEBD code fast and efficient.

Numerical details

The rapidly growing truncation error (the weight of discarded Schmidt states) that spoils the accuracy of TEBD simulations leads to a short cutoff time beyond which results get unreliable. In our simulations, we defined this cutoff time where the truncation error reached 10^{-7}. To reach long enough times ($t \gtrsim \tau$), the MPS bond-dimension was set up to $M_{\text{SU}(2)} = 2000$, i.e., 2000 multiplets (around 10 000 states) with the largest Schmidt values were kept.

APPENDIX B: THE RELATIVISTIC S-MATRIX

In the hybrid semi-semiclassical simulations, the relativistic S-matrix of the low-energy field theory of the $S = 1$ Heisenberg model (namely, the $O(3)$ nonlinear sigma model) was used to describe the collision events. We used the same S-matrix as in Ref. [43], but we transformed it in the more

convenient form:

$$S = \begin{pmatrix} \sigma_2 + \sigma_3 & 0 & 0 & 0 & 0 & 0 & 0 & 0 & 0 \\ 0 & \sigma_3 & 0 & \sigma_2 & 0 & 0 & 0 & 0 & 0 \\ 0 & 0 & \sigma_1 + \sigma_3 & 0 & -\sigma_1 & 0 & \sigma_1 + \sigma_2 & 0 & 0 \\ 0 & \sigma_2 & 0 & \sigma_3 & 0 & 0 & 0 & 0 & 0 \\ 0 & 0 & -\sigma_1 & 0 & \sigma_1 + \sigma_2 + \sigma_3 & 0 & -\sigma_1 & 0 & 0 \\ 0 & 0 & 0 & 0 & 0 & \sigma_3 & 0 & \sigma_2 & 0 \\ 0 & 0 & \sigma_1 + \sigma_2 & 0 & -\sigma_1 & 0 & \sigma_1 + \sigma_3 & 0 & 0 \\ 0 & 0 & 0 & 0 & 0 & \sigma_2 & 0 & \sigma_3 & 0 \\ 0 & 0 & 0 & 0 & 0 & 0 & 0 & 0 & \sigma_2 + \sigma_3 \end{pmatrix} . \tag{B1}$$

Here the (incoming and outgoing) basis states are $\{|+\,+\rangle, |+\,0\rangle, |+\,-\rangle, |0+\rangle, |00\rangle, |0-\rangle, |-\,+\rangle, |-\,0\rangle, |-\,-\rangle\}$, where $\{+, 0, -\}$ stand for the eigenvalues $S^z = \{1, 0, -1\}$ of the particles. In the two-particle basis states, we used the convention that the left and right spin states always stand for the particles in the left and right positions, both in the incoming and outgoing states. The values σ_i depend on the relative rapidity $\theta_{\rm rel} = \theta_1 - \theta_2$ of the colliding particles as

$$\sigma_1 = \frac{2i\pi\theta_{\rm rel}}{(\theta_{\rm rel} + i\pi)(\theta_{\rm rel} - 2i\pi)} ,$$

$$\sigma_2 = \frac{\theta_{\rm rel}(\theta_{\rm rel} - i\pi)}{(\theta_{\rm rel} + i\pi)(\theta_{\rm rel} - 2i\pi)} ,$$

$$\sigma_3 = \frac{-2i\pi(\theta_{\rm rel} - i\pi)}{(\theta_{\rm rel} + i\pi)(\theta_{\rm rel} - 2i\pi)} . \tag{B2}$$

APPENDIX C: PERTURBATIVE DESCRIPTION OF THE QUENCH

In this Appendix, we provide some details on the quench dynamics within our effective field theory, presented in Sec. V.

We shall assume in what follows that our initial quench state is a squeezed state [76,77]. Using that our time-dependent Hamiltonian Eq. (21) is quadratic, one can show that the wave function remains a squeezed state upon time evolution:

$$|\Psi(t)\rangle \sim e^{\sum_{q>0,\sigma}(i\Phi_{q,\sigma}(t) + (-1)^\sigma K_q(t) b_{q,\sigma}^\dagger b_{-q,\bar{\sigma}}^\dagger)}|0\rangle . \tag{C1}$$

The exponential form corresponds to independent pairs of quasiparticles.

Our task is to determine the full time evolution of the functions $K_q(t)$ throughout a quantum quench. First we observe that different momentum modes decouple as

$|\Psi(t)\rangle = \prod_{q>0} |\Psi_q(t)\rangle$, with

$$|\Psi_q(t)\rangle = \sqrt{1 - |K_q|^2}\, e^{i\Phi_q} \sum_{n=0}^{\infty} \frac{1}{n!} K_q^n (b_q^\dagger b_{-q}^\dagger)^n |0\rangle . \tag{C2}$$

The time-dependent Schrödinger equation leads to an equation for the pair creation amplitude K_q,

$$i\dot{K}_q(t) = 2\omega_q(t) K_q(t) + g_q(t)(1 + K_q(t)^2) . \tag{C3}$$

Within first-order perturbation theory, we can neglect the nonlinear $K_q(t)^2$ term in this equation. Using the initial values of the parameters, $\omega_q(t \to -\infty) = \omega_q + J_2 \Delta_q$ and $g_q(t \to -\infty) = J_2 g_q$, and exploiting that in the limit $t \to -\infty$ we initialize the system in its stationary vacuum state, we find the following initial conditions:

$$\lim_{t \to -\infty} K_q(t) = -\frac{J_2 g_q}{2(\omega_q + J_2 \Delta_q)} = -\frac{J_2 g_q}{2\omega_q} + O(J_2^2) . \tag{C4}$$

In general, one needs to solve Eq. (C3) numerically. However, we can easily obtain its approximate analytical solution up to leading order in J_2,

$$\lim_{t \to \infty} K_q(t) = \frac{J_2 g_q}{2\omega_q} e^{-2i\omega_q t} \int_{-\infty}^{\infty} dt'\, \dot{\lambda}(t') e^{2i\omega_q t'} + O(J_2^2) . \tag{C5}$$

Using this expression, we find that the density of quasiparticles created by the quench is just given by Eq. (23).

For the particular quench profile,

$$\lambda(t) = \tfrac{1}{2}[1 - \tanh(t/t_Q)], \tag{C6}$$

the Fourier transformation can be performed analytically with the result

$$n(q) = \frac{\pi^2}{4} \frac{J_2^2 g_q^2 t_Q^2}{4 \sinh^2(\pi \omega_q t_Q)} . \tag{C7}$$

For slow enough quenches, the denominator cuts off the momentum distribution at low momenta, so we can substitute g_q with its small momentum behavior, $g_q \approx g\,|q|$, and we obtain the momentum distribution Eq. (25).

[1] M. A. Cazalilla and M. Rigol, New J. Phys. **12**, 055006 (2010).

[2] A. Polkovnikov, K. Sengupta, A. Silva, and M. Vengalattore, Rev. Mod. Phys. **83**, 863 (2011),

[3] J. Eisert, M. Friesdorf, and C. Gogolin, Nat. Phys. **11**, 124 (2015).

[4] P. Calabrese, F. H. L. Essler, and G. Mussardo, J. Stat. Mech. (2016) 064001.

[5] T. Prosen, J. Phys. A: Math. Theor. **48**, 373001 (2015).

[6] D. Bernard and B. Doyon, J. Stat. Mech. (2016) 064005.

[7] B. Bertini and M. Fagotti, Phys. Rev. Lett. **117**, 130402 (2016).

[8] M. Collura, A. De Luca, and J. Viti, Phys. Rev. B **97**, 081111(R) (2018).

[9] M. Moeckel and S. Kehrein, Phys. Rev. Lett. **100**, 175702 (2008).

[10] B. Bertini, F. H. L. Essler, S. Groha, and N. J. Robinson, Phys. Rev. Lett. **115**, 180601 (2015).

[11] P. Calabrese and J. Cardy, J. Stat. Mech. (2005) P04010.

[12] N. Schuch, M. M. Wolf, F. Verstraete, and J. I. Cirac, Phys. Rev. Lett. **100**, 030504 (2008).

[13] V. Alba and P. Calabrese, PNAS **114**, 7947 (2017).

[14] A. Nahum, J. Ruhman, S. Vijay, and J. Haah, Phys. Rev. X **7**, 031016 (2017).

[15] M. Collura, M. Kormos, and G. Takács, Phys. Rev. A **98**, 053610 (2018).

[16] M. Žnidaric, T. Prosen, and P. Prelovšek, Phys. Rev. B **77**, 064426 (2008).

[17] J. H. Bardarson, F. Pollmann, and J. E. Moore, Phys. Rev. Lett. **109**, 017202 (2012).

[18] A. Nanduri, H. Kim, and D. A. Huse, Phys. Rev. B **90**, 064201 (2014).

[19] M. Serbyn, Z. Papić, and D. A. Abanin, Phys. Rev. B **90**, 174302 (2014).

[20] R. Vasseur and J. E. Moore, J. Stat. Mech. (2016) 064010.

[21] G. B. Halász and A. Hamma, Phys. Rev. Lett. **110**, 170605 (2013).

[22] L. Mazza, D. Rossini, M. Endres, and R. Fazio, Phys. Rev. B **90**, 020301(R) (2014).

[23] L. D'Alessio and M. Rigol, Nat. Commun. **6**, 8336 (2015).

[24] M. McGinley and N. R. Cooper, Phys. Rev. Lett. **121**, 090401 (2018).

[25] T. Kinoshita, T. Wenger, and D. S. Weiss, Nature **440**, 900 (2006).

[26] S. Trotzky, Y.-A. Chen, A. Flesch, I. P. McCulloch, U. Schollwöck, J. Eisert, and I. Bloch, Nat. Phys. **8**, 325 (2012).

[27] M. Gring, M. Kuhnert, T. Langen, T. Kitagawa, B. Rauer, M. Schreitl, I. Mazets, D. A. Smith, E. Demler, and J. Schmiedmayer, Science **337**, 1318 (2012).

[28] M. Cheneau, P. Barmettler, D. Poletti, M. Endres, P. Schaua, T. Fukuhara, C. Gross, I. Bloch, C. Kollath, and S. Kuhr, Nature **481**, 484 (2012).

[29] T. Langen, R. Geiger, and J. Schmiedmayer, Annu. Rev. Condens. Matter Phys. **6**, 201 (2015).

[30] A. M. Kaufman, M. E. Tai, A. Lukin, M. Rispoli, R. Schittko, P. M. Preiss, and M. Greiner, Science **353**, 794 (2016).

[31] V. E. Korepin, A. G. Izergin, and N. M. Bogoliubov, *Quantum Inverse Scattering Method, Correlation Functions and Algebraic Bethe Ansatz* (Cambridge University Press, Cambridge, UK, 1993).

[32] F. D. M. Haldane, J. Phys. C **14**, 2585 (1981).

[33] T. Giamarchi, *Quantum Physics in One Dimension* (Clarendon Press, Oxford, UK, 2003).

[34] S. R. White, Phys. Rev. Lett. **69**, 2863 (1992).

[35] U. Schollwöck, Annals of Physics **326**, 96 (2011).

[36] T. Prosen and M. Žnidarič, J. Stat. Mech. (2009) P02035.

[37] J. Cui, J. I. Cirac, and M.-C. Bañuls, Phys. Rev. Lett. **114**, 220601 (2015).

[38] S. R. White and A. E. Feiguin, Phys. Rev. Lett. **93**, 076401 (2004).

[39] G. Vidal, Phys. Rev. Lett. **98**, 070201 (2007).

[40] C. P. Moca, M. Kormos, and G. Zaránd, Phys. Rev. Lett. **119**, 100603 (2017).

[41] S. Sachdev and A. P. Young, Phys. Rev. Lett. **78**, 2220 (1997).

[42] S. Sachdev and K. Damle, Phys. Rev. Lett. **78**, 943 (1997).

[43] M. Kormos, C. P. Moca, and G. Zaránd, Phys. Rev. E **98**, 032105 (2018).

[44] K. Damle and S. Sachdev, Phys. Rev. Lett. **95**, 187201 (2005).

[45] Á. Rapp and G. Zaránd, Phys. Rev. B **74**, 014433 (2006).

[46] S. Evangelisti, J. Stat. Mech. (2013) P04003.

[47] M. Kormos and G. Zaránd, Phys. Rev. E **93**, 062101 (2016).

[48] M. A. Werner, C. P. Moca, Ö. Legeza, and G. Zaránd (unpublished).

[49] R. Orús, Annals of Physics **349**, 117 (2014).

[50] E. Schmidt, Math. Ann. **63**, 433 (1907).

[51] I. P. McCulloch and M. Gulácsi, Europhys. Lett. **57**, 852 (2002).

[52] S. Singh, H.-Q. Zhou, and G. Vidal, New J. Phys. **12**, 033029 (2010).

[53] The state $|t, \overline{m}\rangle_{\text{right}}$ stands for the Schmidt pair of $|t, m\rangle_{\text{left}}$. The specific form Eq. (4) of the Schimdt decomposition of a pure state relies on the orthogonality relation of representation characters and is correct only for singlet states (see also Refs. [48,51,52]).

[54] In higher symmetries like SU(N), the η-leg is not only used to match the three spin indices between the $A^{[l]}$ and C tensors, but can also handle the so-called outer multiplicities in the generalized Clebsch–Gordan series. The two-layer structure is similar to other non-Abelian MPS approaches presented, e.g., in Refs. [52,75], but the formal introduction of the η-leg makes our approach different from them.

[55] H. F. Trotter, Proc. Am. Math. Soc. **10**, 545 (1959).

[56] M. Suzuki, Commun. Math. Phys. **51**, 183 (1976).

[57] F. D. M. Haldane, Phys. Rev. Lett. **50**, 1153 (1983).

[58] S. R. White and I. Affleck, Phys. Rev. B **77**, 134437 (2008).

[59] More precisely, one should consider the equivalent of the thermal de Broglie wavelength which is related to the momentum of the particles. We estimate that for the quenches considered here, the "thermal" wavelength is comparable with the Compton wavelength.

[60] I. Affleck, T. Kennedy, E. H. Lieb, and H. Tasaki, Phys. Rev. Lett. **59**, 799 (1987).

[61] T. Kennedy, J. Phys.: Condens. Matter **2**, 5737 (1990).

[62] In Eq. (11), the spin factors just originate from the observation that the probability distribution in the $(2S_0 + 1)(2S_{\text{qp}} + 1)$-dimensional product space of S_0 and $2S_{\text{qp}}$ is uniform, and therefore the probability of forming a spin S state—allowed by the addition rules—is just proportional to its degeneracy, $2S + 1$, and is equal to $(2S + 1)/[(2S_0 + 1)(2S_{\text{qp}} + 1)]$.

[63] The same structure appears for quenches in the transverse field Ising chain [M. Heyl, A. Polkovnikov, and S. Kehrein, Phys. Rev. Lett. **110**, 135704 (2013)]; and in Luttinger liquids [B. Dóra, M. Haque, and G. Zaránd, *ibid.* **106**, 156406 (2011)].

[64] B. L. Altshuler, R. M. Konik, and A. M. Tsvelik, Nucl. Phys. B **739**, 311 (2006).

[65] A. Rapp, P. Schmitteckert, G. Takacs, and G. Zarand, New J. Phys. **15**, 013058 (2013).

[66] L. Vanderstraeten, J. Haegeman, T. J. Osborne, and F. Verstraete, Phys. Rev. Lett. **112**, 257202 (2014).

[67] S. Gustavsson, R. Leturcq, B. Simovič, R. Schleser, T. Ihn, P. Studerus, K. Ensslin, D. C. Driscoll, and A. C. Gossard, Phys. Rev. Lett. **96**, 076605 (2006).

[68] A. Lamacraft and P. Fendley, Phys. Rev. Lett. **100**, 165706 (2008).

[69] S. Hofferberth, I. Lesanovsky, T. Schumm, A. Imambekov, V. Gritsev, E. Demler, and J. Schmiedmayer, Nat. Phys. **4**, 489 (2008).

[70] T. B. Batalhão, A. M. Souza, L. Mazzola, R. Auccaise, R. S. Sarthour, I. S. Oliveira, J. Goold, G. De Chiara, M. Paternostro, and R. M. Serra, Phys. Rev. Lett. **113**, 140601 (2014).

[71] I. Lovas, B. Dóra, E. Demler, and G. Zaránd, Phys. Rev. A **95**, 053621 (2017).

[72] M. Collura, F. H. L. Essler, and S. Groha, J. Phys. A **50**, 414002 (2017).

[73] H. R. Krishna-murthy, J. W. Wilkins, and K. G. Wilson, Phys. Rev. B **21**, 1003 (1980).

[74] C. P. Moca, A. Alex, J. von Delft, and G. Zaránd, Phys. Rev. B **86**, 195128 (2012).

[75] A. Weichselbaum, Annals of Physics **327**, 2972 (2012).

[76] D. Fioretto and G. Mussardo, New J. Phys. **12**, 055015 (2010).

[77] D. X. Horváth, S. Sotiriadis, and G. Takács, Nucl. Phys. B **902**, 508 (2016).